Available online at www.sciencedirect.com

ScienceDirect

Journal of Magnesium and Alloys 11 (2023) 4181–4188

www.elsevier.com/locate/jma

Full Length Article

Bi nanoparticles encapsulated in nitrogen-doped carbon as a long-life anode material for magnesium batteries

Junjun Wang[a,b], Ruohan Yu[a], Jianxiang Wang[a], Juncai Long[a], Fan Qiao[a], Lei Zhang[a], Guanjie He[b], Qinyou An[a,c,*], Liqiang Mai[a,c,*]

[a] State Key Laboratory of Advanced Technology for Materials Synthesis and Processing, School of Materials Science and Engineering, Wuhan University of Technology, Wuhan 430070, China

[b] Christopher Ingold Laboratory, Department of Chemistry, University College London, 20 Gordon Street, London WC1H 0AJ, United Kingdom of Great Britain and Northern Ireland, United Kingdom

[c] Hubei Longzhong Laboratory, Wuhan University of Technology (Xiangyang Demonstration Zone), Xiangyang 441000, China

Received 27 September 2023; received in revised form 22 October 2023; accepted 30 October 2023

Available online 5 December 2023

Abstract

Bismuth has garnered significant interest as an anode material for magnesium batteries (MBs) because of its high volumetric specific capacity and low working potential. Nonetheless, the limited cycling performance (≤100 cycles) limits the practical application of Bi as anode for MBs. Therefore, the improvement of Bi cycling performance is of great significance to the development of MBs and is also full of challenges. Here, Bi nanoparticles encapsulated in nitrogen-doped carbon with single-atom Bi embedded (Bi@NC) are prepared and reported as an anode material for MBs. Bi@NC demonstrates impressive performance, with a high discharge capacity of 347.5 mAh g^{-1} and good rate capability (206.4 mAh g^{-1}@500 mA g^{-1}) in a fluoride alkyl magnesium salt electrolyte. In addition, Bi@NC exhibits exceptional long-term stability, enduring 400 cycles at 500 mA g^{-1}. To the best of our knowledge, among reported Bi and Bi-based compounds for MBs, Bi@NC exhibits the longest cycle life in this work. The magnesium storage mechanism of Bi@NC is deeply studied through X-ray diffraction, transmission electron microscopy and X-ray photoelectron spectroscopy. This work provides some guidance for further improving the cycling performance of other alloy anodes in MBs.

Keywords: Magnesium batteries; Bismuth; 3D tomography reconstruction; Magnesium alloy; Single-atom.

1. Introduction

The low raw material reserves (Co, Li, and Ni) make it difficult for lithium-ion batteries (LIBs) to be used in large-scale energy storage for a long time, which drives researchers to develop energy storage devices based on abundant materials [1–3]. Due to the abundant reserves, moderate redox potential, and high volumetric (3833 mAh cm^{-3}) and gravimetric (2205 mAh g^{-1}) specific capacities of Mg, magnesium batteries (MBs) have gained significant attention as a promising candidate for post-LIBs [4–6]. In addition, as Mg is less prone to dendrite formation and thermal runaway, MBs may have safety advantages over LIBs [7,8]. Therefore, MBs have good application prospects in large-scale energy storage. However, the high reactivity of Mg metal and the slow diffusion kinetics of Mg^{2+} make the metal Mg anode easily passivated in most Mg electrolytes [9], which seriously limits the development and application of MBs. To overcome this challenge, researchers have adopted many strategies, including regulating the solvation structure of Mg^{2+} [8,10,11], designing and constructing solid electrolyte interfaces [12,13], and developing alloy anodes [14]. Among them, alloy an-

* Corresponding authors at: State Key Laboratory of Advanced Technology for Materials Synthesis and Processing, School of Materials Science and Engineering, Wuhan University of Technology, Wuhan 430070, China

E-mail addresses: anqinyou86@whut.edu.cn (Q. An), mlq518@whut.edu.cn (L. Mai).

https://doi.org/10.1016/j.jma.2023.10.001

odes (such as Bi [15], Sn [16], Ga [17], etc.) have garnered significant attention from researchers in the past decade due to their high specific capacity and low working potential, and have the potential to become an alternative to Mg metal anode [14].

Among alloy anodes, due to the high volumetric capacity (3783 mAh cm^{-3}) and favorable reaction kinetics of Bi metal at room temperature, Bi and Bi-based compounds have been widely studied as anode for MBs. For instance, Masaki et al. [18] reported $Bi_{1-x}Sb_x$ and Bi as anodes for MBs in 2012 and Bi maintained a capacity of 222 mAh g^{-1} after 100 cycles. Grey et al. [19] et al. studied the magnesium storage mechanism of Bi through solid-state nuclear magnetic resonance spectroscopy in 2017. In 2018, Munichandraiah et al. [20] improved the cycling and rate performance of Bi through the composite of Bi and reduced graphene oxide (Bi/rGO) and Bi/rGO, after 50 cycles, showed a capacity of 372 mAh g^{-1}. Zhang et al. [16,21,22] reported that the rate performance and discharge capacity of Bi were significantly improved through Bi-Sn dual-phase alloy engineering, up to 362 mAh g^{-1} at 1 A g^{-1}. Recently, Zhao et al. [15] further improved the rate performance of Bi to 218 mAh g^{-1}@3 A g^{-1} through material structure design. In addition, polyaniline intercalated $Bi_2O_2CO_3$, BiOF and BiOCl were reported as anode materials for MBs and delivered the cycling stability of 300, 100 and 100 cycles, respectively [23–25]. Unfortunately, Bi and Bi-based compounds, as anodes for MBs, still exhibit poor cycling performance. In particular, the longest reported life of the Bi metal anode is 100 cycles. In the past, to enhance the cycling performance of Bi anode, researchers primarily focused on improving material structures to mitigate the significant volume expansion (104%) during alloy reactions [15,26,27]. However, the influence of electrolyte on the performance of electrode materials was overlooked, and the magnesium storage performance of most Bi or Bi-based compounds was evaluated in traditional all phenyl complex (APC) electrolytes. Therefore, simultaneously considering the influence of the electrolyte on performance while designing material structures may be an effective strategy for enhancing the cycling performance of Bi anodes.

In this work, Bi nanoparticles encapsulated in nitrogen-doped carbon with single-atom Bi embedded (Bi@NC) are prepared by low temperature calcination method and used as anode materials for MBs in a fluoride alkyl Mg salt electrolyte. The structure of Bi@NC is thoroughly characterized by spherical aberration-corrected scanning transmission electron microscopy (STEM) and three-dimensional (3D) tomography reconstruction techniques. Benefiting from the unique structure of Bi@NC and the excellent stability of electrolyte, Bi@NC exhibits a high discharge capacity of 347.5 mAh g^{-1}, 82.5% high capacity retention after 400 cycles and good rate capability (206.4 mAh g^{-1}@500 mA g^{-1}). Furthermore, the magnesium storage mechanism of Bi@NC is shown to involve an alloying reaction from Bi to Bi_2Mg_3 through X-ray diffraction (XRD), X-ray photoelectron spectroscopy (XPS) and TEM.

2. Experimental section

2.1. Material preparation

Preparation of flower-like $Bi_2O_2CO_3$ (BOC). The BOC was prepared by hydrothermal method [28]. Firstly, sodium citrate dihydrate (Aladdin, 5 mmol) and $Bi(NO_3)_2{\cdot}5H_2O$ (Macklin, 5 mmol) were added to 60 mL ultrapure water and the obtained solution was sonicated and stirred at room temperature for 30 min. Afterward, 30 mmol of urea (Aladdin) was added to the above solution. The obtained solution was continued to be sonicated and stirred for 30 min. Then, the sealed autoclave (100 mL) was kept at 150 °C for 12 h. Finally, the BOC was collected by centrifugation and washing with deionized water and ethanol, and finally dried for 12 h at 60 °C.

Synthesis of Bi@NC. Bi@NC are prepared by low temperature calcination method [29]. The prepared BOC flower (100 mg) was added into 150 mL tris-buffer solution (10 mM) and sonicated for 10 min. Then, 100 mg dopamine hydrochloride (PDA, Aladdin) were added to the above solution and the solution was stirred for 3 h. The product was collected by centrifugation and washing with deionized water and ethanol. The prepared product was further calcined at 400 °C for 2 h with Ar atmosphere to obtain Bi@NC.

2.2. Material characterizations

Powder and *ex-situ* XRD measurement were performed using a Bruker AXS D2 Advance powder X-ray diffractometer. Scanning electron microscope (SEM) images were acquired by using a JEOL-7100F microscope. The TEM/STEM images and EDX spectra experiments were collected using a CEOS probe corrected FEI Themis TEM (electron accelerating voltage is 300 kV) equipped with a Gatan image filter spectrometer. Electron tomography experiments were performed on a Fischione tomography holder with a −75° to +75° tilt range. The reconstruction was performed using the Thermo Fisher 3D Inspect and visualized in Avizo. Kratos AXIS SUPRA instrument was used for XPS measurement. Thermogravimetric analysis (TGA) was carried out on a NETZSCH-STA449F3 thermo-analyzer with a heating rate of 10 °C min^{-1} and air atmosphere.

2.3. Electrochemical experiments

Preparation of electrodes. The electrode consisting of Bi@NC or BOC (60 wt%), acetylene black (AB, 30 wt%), and poly(vinylidene fluoride (PVDF, 10 wt%). They were mixed and dispersed in Nmethyl-2-pyrrolidinone to form a slurry, and the slurry was cast onto Cu foil and dried at 70 °C for 24 h.

Preparation of electrolytes. 0.4 M APC electrolyte and glyme (DME) were purchased from Suzhou Industrial Park Sange Chemical Technology Co., Ltd. The fluoride alkyl Mg salt ($Mg(PFTB)_2$) electrolyte was prepared based on our previous work [30]. In an argon filled glovebox, $AlCl_3$ (2 mmol)

was dissolved in 5 mL DME. Then, $Mg(PFTB)_2$ (1 mmol) was added into the above solution. After magnetic stirring at room temperature for minutes, a clear solution was obtained. Finally, $MgCl_2$ (1 mmol) was added to the above solution and stirred at 60 °C for 12 h to obtain a clear and colorless solution. The $Mg(PFTB)_2$ electrolyte was obtained.

The magnesium storage performance test for Bi@NC and BOC. The magnesium storage performances of Bi@NC and BOC were tested by CR2016 coin cell assembled with the prepared electrodes, GF/A as separator, APC electrolyte or $Mg(PFTB)_2$ electrolyte. The active materials loading on the cathode (10 mm diameter) is about 1.0 mg cm^{-2}. All electrochemical performance tests were carried out at room temperature. The LAND CT2001A and NEWARE multichannel battery testing systems were used for cycling performance and rate performance test. Cyclic voltammetry (CV) tests were performed with an Autolab PGSTAT 302 N electrochemical workstation.

3. Result and discussion

The XRD patterns of both the prepared BOC and Bi@NC materials are presented in Fig. 1a. It is evident that all diffraction peaks from BOC can be attributed to the tetragonal $Bi_2O_2CO_3$ (PDF#41–1488, I4/mmm). The XRD pattern of Bi@NC can also be well indexed to the hexagonal Bi (PDF#44–1246, R-3m). The results indicate that pure-phase BOC and Bi@NC have been successfully prepared. The crystal structures corresponding to BOC and Bi@NC are shown in Fig. 1b and c respectively. The structure of BOC consists of alternating stacking layers of $(Bi_2O_2)^{2+}$ and CO_3^{2-}. The crystal structure of Bi is a typical metallic structure and contains only metallic bonds. The SEM and TEM images show that the morphology of BOC is a flower composed of nanosheets (Figs. 1d and S1) and the morphology of Bi@NC derived from BOC is nanoparticles (Fig. S2). The morphology and structural characteristics of Bi@NC were further analyzed by TEM. The bright-field (BF) and high-angle annular dark-field (HAADF)-STEM images of the Bi@NC (Fig. 1e and f) indicate that Bi nanoparticles are encapsulated by carbon derived from the pyrolysis of PDA. The high magnification HAADF-STEM image of Bi@NC is shown in Fig. 1g and the bright dots in the HAADF-STEM image are assigned to Bi atoms and the position of Bi atoms is consistent with the crystal structure of Bi along *b* direction. The HAADF-STEM image of Bi@NC shows that the interplanar spacing is 3.3 Å, corresponding to the (012) crystal plane of Bi. The HAADF image of Bi@NC with elemental maps (Fig. 1h) show the distribution of Bi, C and N elements. The energy dispersive X-ray (EDX) spectrum of Bi@NC (Fig. S3) further confirms the presence of Bi, C and N elements. Furthermore, the presence of N and C elements was analyzed through XPS. Fig. 1i shows the XPS spectra of N 1 s for Bi@NC and the three peaks correspond to pyridinic-N, pyrrolic-N and quaternary-N, respectively [31]. The XPS spectra of C 1 s and O 1 s for Bi@NC are shown in Fig. S4, indicating the presence of C–N and Bi-O bonds. The wide XPS spectrum of Bi@NC also indicates the presence of Bi, C, O and N elements (Fig. S5). The XPS spectra of C, N and O elements for BOC are also displayed in Fig. S6. The presence of N element is due to the addition of urea during the synthesis process. The Raman spectra of Bi@NC (Fig. 1j) proves the presence of carbon, and the result of TGA shows the carbon content is 17.8% (Fig. S7) [32]. However, the peaks corresponding to carbon are not observed in the Raman spectrum of BOC (Fig. S8).

To observe the encapsulation structure and form of carbon in Bi@NC, HAADF-STEM images of Bi@NC with Bi and carbon layer is shown in Fig. 2a. We can observe that the carbon layer is in close contact with the Bi particles at the interface, which is beneficial to improving the electronic conductance of Bi and buffering large volume changes during the electrochemical process. Surprisingly, in the HAADF-STEM image of carbon layer (Fig. 2b), we can find that a large number of Bi single atoms or clusters are embedded into the carbon, which may enhance the reaction kinetics of Bi to a certain extent. The presence of Bi single atoms can also be observed in other carbon layers (Fig. S9). In addition, the XPS spectra of Bi 4f (Fig. 2c) shows that the valence state of Bi for Bi@NC is +3, which is the same as the valence state of Bi in BOC (Fig. S10). The observation of Bi^{3+} for Bi@NC may be caused by the presence of single-atom Bi or Bi_2O_3 on the particle surface. Combined with the TEM results, the presence of single-atom Bi in Bi@NC can be further confirmed by XPS.

To further demonstrate the encapsulation form of carbon in Bi@NC, 3D tomography reconstruction was used. A set of 75 HAADF-STEM images (Fig. 2d) was obtained within a range of 150° with an interval of 2° for tomography reconstruction. The reconstructed Bi@NC model is shown in Fig. 2e and f. According to the different HAADF contrasts of Bi and C elements, the color of the corresponding carbon and Bi nanoparticles in the reconstructed Bi@NC model is adjusted to translucent green and orange, respectively. The reconstructed Bi@NC model with different colors (Fig. 2e and Supplementary Video 1) indicates that Bi nanoparticles are encapsulated within a 3D carbon structure, which can be further shown by the three views in Fig. 2f and the orthoslices (Fig. 2g). Based on the contrast differences, the carbon shell and individual Bi nanoparticles in Bi@NC are represented using different colors (Fig. 2h and i, Supplementary Video 2). The reconstructed models of Bi nanoparticles and carbon shells are illustrated in Fig. 2j and Fig. 2k, respectively. Notably, the carbon shell is continuous (Fig. 2l), and some isolated Bi nanoparticles can be encapsulated together by the continuous carbon shell, effectively improving the electronic conductivity of Bi and buffer volume changes. The above results indicate that Bi nanoparticles encapsulated in nitrogen-doped carbon with single-atom Bi embedded was successfully prepared.

The magnesium storage performance of Bi@NC and BOC were evaluated in APC electrolyte and $Mg(PFTB)_2$ electrolyte. The rate performance of Bi@NC and BOC, in $Mg(PFTB)_2$ electrolyte, are depicted in Fig. 3a and the

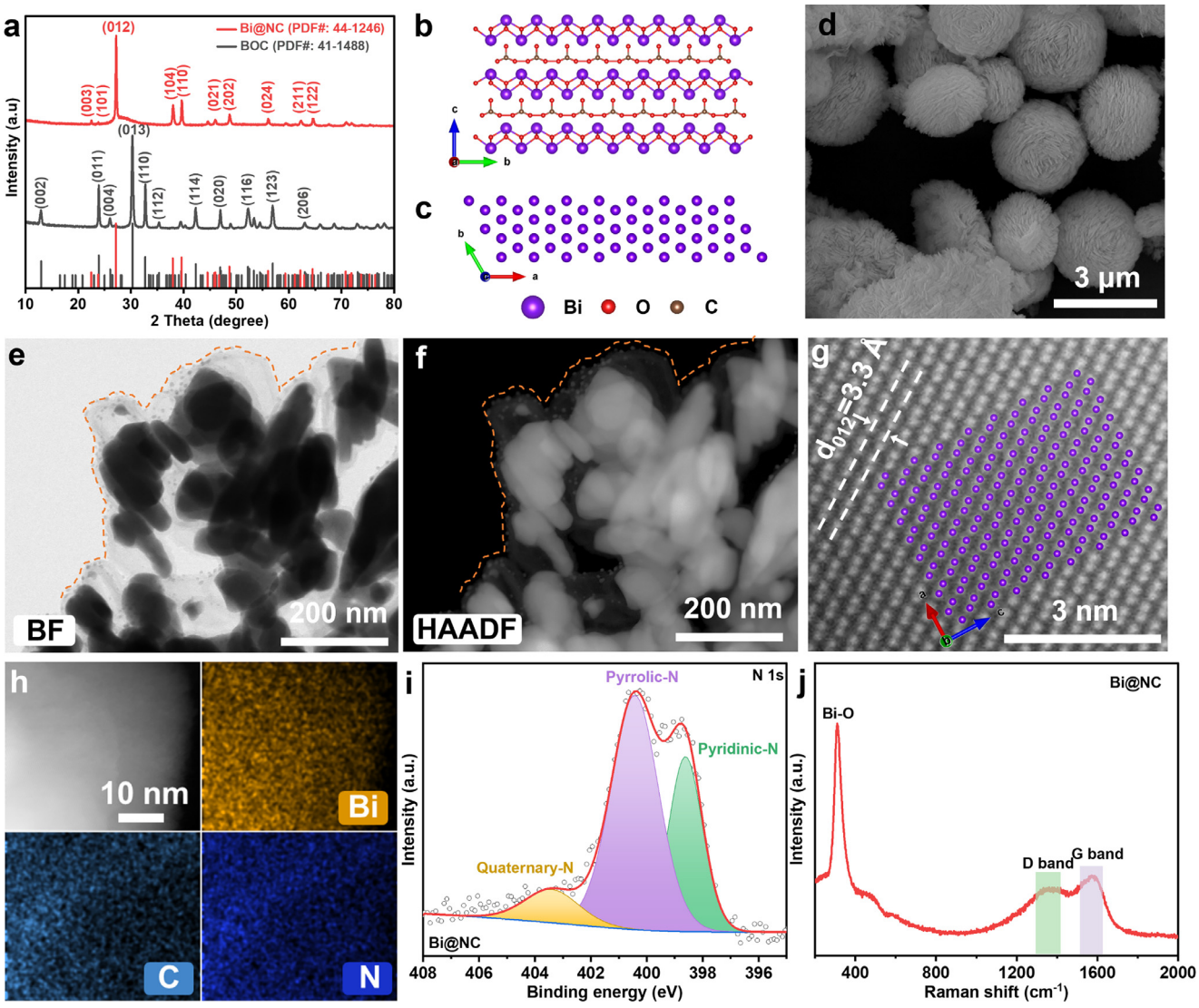

Fig. 1. (a) XRD patterns of BOC and Bi. Crystal structures of (b) BOC and (c) Bi. (d) SEM image of BOC. (e) BF-STEM and (f) HAADF-STEM images of Bi@NC. (g) HAADF-STEM images of Bi@NC and corresponding crystal structure along *b* direction. (h) HAADF image of Bi@NC and corresponding elemental maps. (i) N 1 s XPS spectra of Bi@NC. (j) Raman spectra of Bi@NC.

corresponding charge-discharge curves at various current are provided in Figs. S11 and S12. At 100 mA g^{-1}, Bi@NC delivers a high capacity of 347.5 mAh g^{-1}. Even at 500 mA g^{-1}, Bi@NC exhibits a discharge capacity of 206.4 mAh g^{-1}, indicating good rate performance. However, as the precursor of Bi@NC, BOC exhibits poor rate performance (only 63.9 mAh g^{-1}@500 mA g^{-1}) in $Mg(PFTB)_2$ electrolyte. Fig. 3b shows the charge-discharge profiles of BOC and Bi@NC at 200 mA g^{-1} and it can be observed that Bi@NC exhibits a smaller overpotential and higher capacity. The charge-discharge curve of Bi@NC for the first cycle is shown in Fig. S13. For comparison, the magnesium storage performance of Bi@NC and BOC were also tested in APC electrolyte. Bi@NC only has a low capacity of 2.1 mAh g^{-1} even at 50 mA g^{-1} (Fig. S14). BOC exhibits a discharge capacity of 155.9 mAh g^{-1} at 100 mA g^{-1} in APC electrolyte (Fig. S15), which is close to the capacity of BOC in $Mg(PFTB)_2$ electrolyte. The results demonstrate that electrolyte formulations have a huge impact on electrode material performance. Therefore, the compatibility of electrolytes and electrode materials should also be considered while improving or designing the structure of electrode materials. Fig. 3c exhibits the cycling performance of Bi@NC in $Mg(PFTB)_2$ electrolyte at 200 mA g^{-1}. The low Coulombic efficiency at the first cycle may be caused by the presence of Bi^{3+} in Bi@NC (Fig. 2c). Bi@NC has a specific capacity of 289.4 mAh g^{-1} and 300 cycles with 74.7% capacity retention. Bi@NC can also demonstrate a high specific capacity of 263.4 mAh g^{-1} (Fig. 3d) and a long life of 400 cycles with a high capacity retention of 82.5% (Fig. 3e) at 500 mA g^{-1}. Compared with the Mg^{2+} storage performance of Bi@NC with reported Bi and Bi-based compounds for MBs (Fig. 3f), Bi@NC exhibits longest cycle life, which is closely related to the stability of the material structure and the electrolyte.

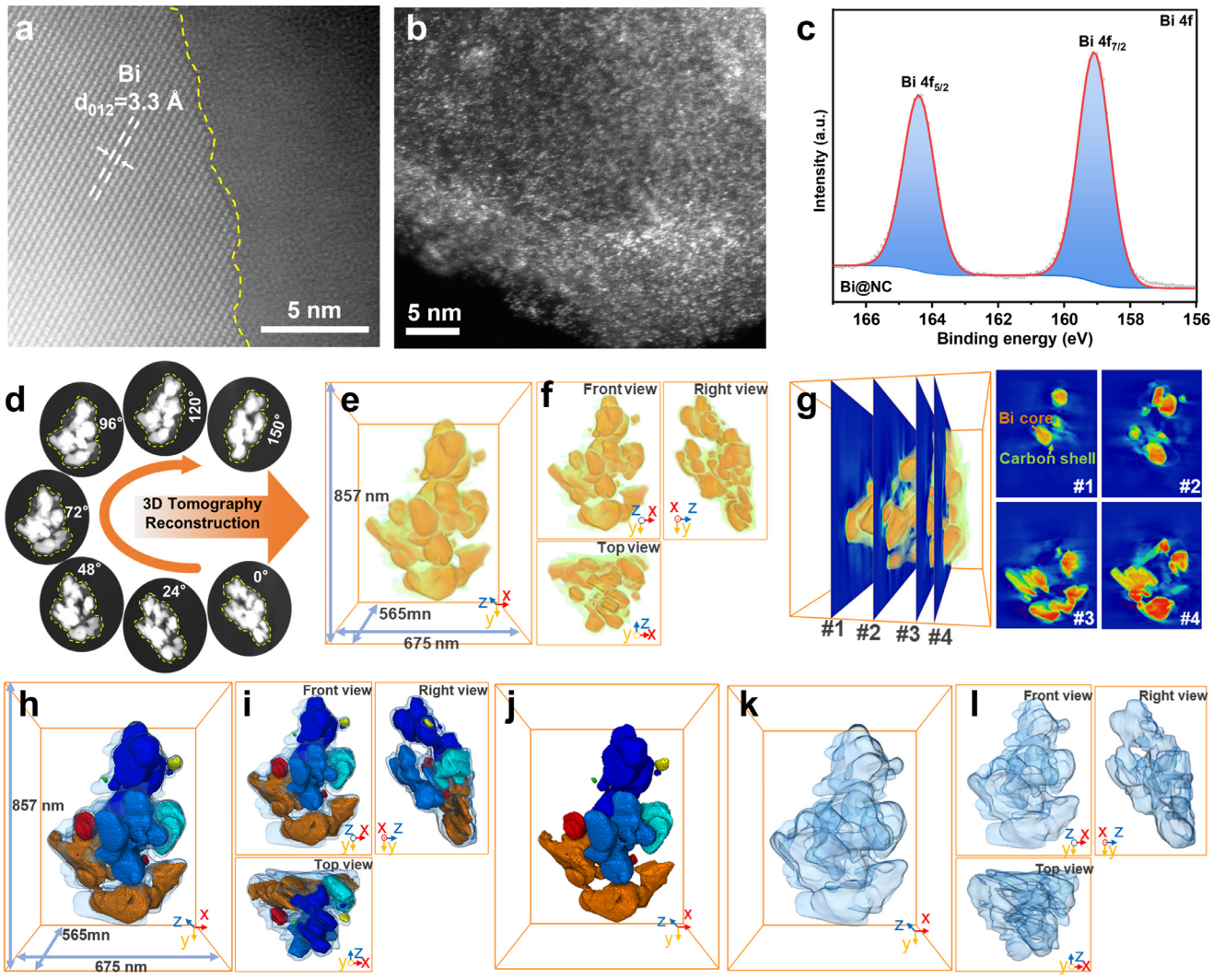

Fig. 2. (a) and (b) HAADF-STEM images of Bi@NC at different area. (c) Bi 4f XPS spectra of Bi@NC. (d) HAADF-STEM images of Bi@NC at different rotation angles. (e) 3D visualization of tomographic reconstruction images of Bi@NC model and (f) the corresponding front, top, and right views. (g) The orthoslicing images of Bi@NC. (h-l) Analysis of carbon shell and Bi nanoparticle distribution in Bi@NC by 3D tomography reconstruction techniques.

To study the reaction kinetic of Mg^{2+} in Bi@NC, the multiple scan rate CV curves are collected from 0.2 to 0.8 mV s^{-1} (Fig. 3g). CV curve of Bi@NC for the first cycle is shown in Fig. S16. The cathodic and anodic peaks shifted slightly with the increasing scan rate from 0.2 to 0.8 mV s^{-1}, suggesting excellent reaction kinetic. By analyzing the multi-scan CV curves according to the Eq. (1): [33]

$$i = av^b \quad (1)$$

i is the peak current and v is the scan rate. a and b are variables in the Eq. (1). Thereinto, b=0.5 and b=1 means diffusion dominated and capacitive controlled charge storage, respectively. In Fig. 3h, the b values for peak 1 and peak 2 are 0.35 and 0.32 respectively, which indicate that the diffusion process played a dominated role in Bi@NC.

The magnesium storage mechanisms of Bi@NC and BOC in Fig. 4 are revealed through various characterizations. The *ex-situ* XRD patterns of Bi@NC at different states (Fig. 4a and b) shows that, as the discharge process proceeds, some new diffraction peaks corresponding to Bi_2Mg_3 are observed. At the end of charging, the diffraction peak of Bi_2Mg_3 disappears and all diffraction peaks can be indexed to Bi@NC. The results demonstrate that the magnesium storage mechanism of Bi@NC is an alloying reaction based on the transformation of Bi to Bi_2Mg_3. The *ex-situ* XRD patterns of BOC (Fig. S17) show that the diffraction peaks observed at the fully discharged can be indexed to hexagonal Bi (PDF#44–1246, R-3m), indicating that the magnesium storage mechanism of BOC is a two-phase transformation reaction. However, at the fully charged, most of the diffraction peaks do not return to their initial positions and hexagonal Bi diffraction peaks are still observed, which show that BOC exhibits poor reversibility. The XPS spectra of Mg 1 s (Fig. 4c) and the full wide XPS spectra (Fig. S18) for Bi@NC at different states confirm the insertion and extraction of Mg^{2+} during the electrochemical process. The Mg^{2+} insertion and extraction of BOC are

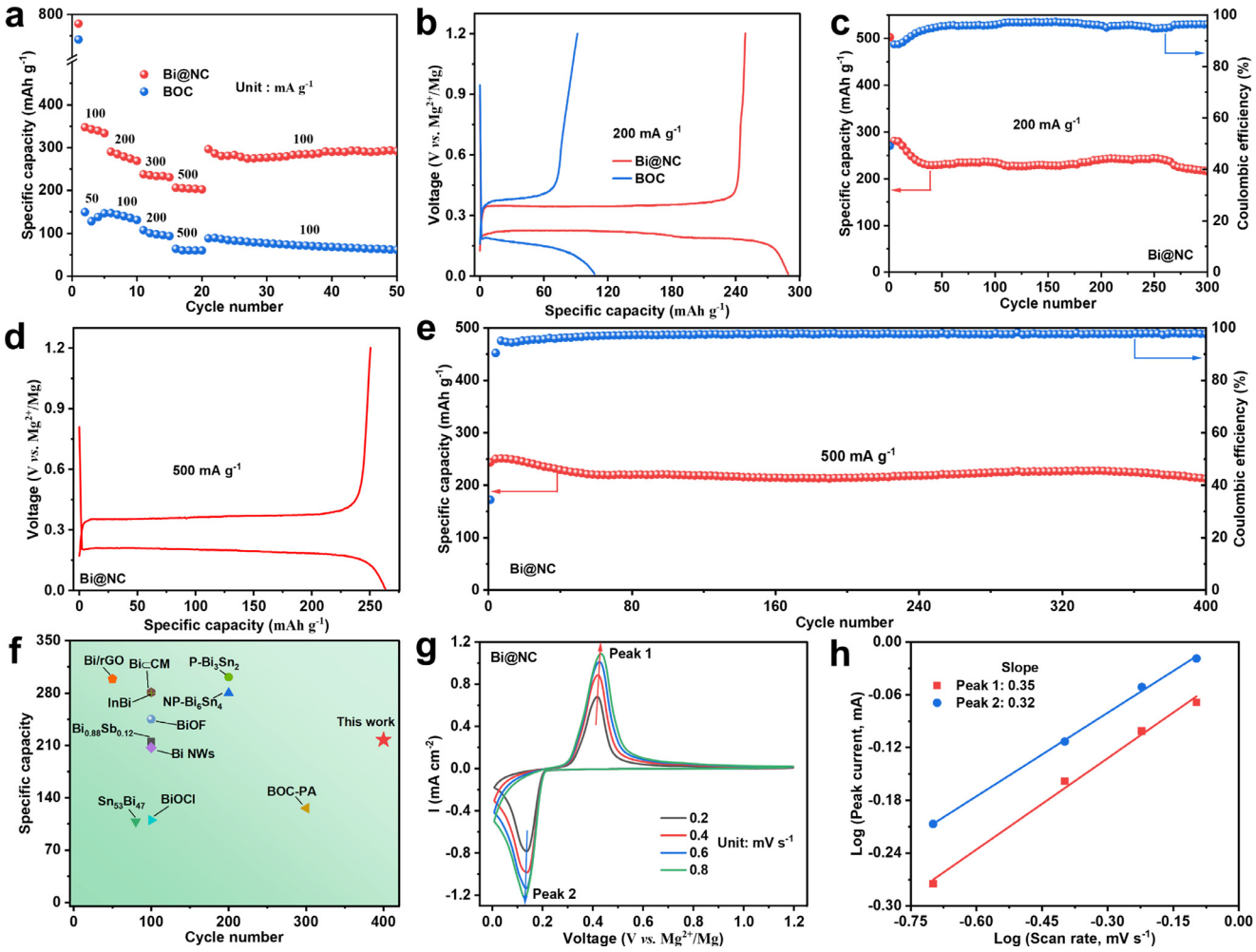

Fig. 3. (a) Rate performance of Bi@NC and BOC. (b) Charge-discharge curves of Bi@NC and BOC at 200 mA g^{-1}. (c) Cycling performance of Bi@NC at 200 mA g^{-1}. Charge-discharge curve (d) and cycling performance (e) of Bi@NC at 500 mA g^{-1}. (f) Comparison of Mg^{2+} storage performance of Bi@NC with reported Bi and Bi-based compounds for MBs [15,16,18-21,23-25]. (g) The CV curves of Bi@NC at different scan rates. (h) Log(i) versus log(v) plots of two redox peaks in CV curves. (For interpretation of the references to colour in this figure legend, the reader is referred to the web version of this article.)

also demonstrated through the Mg 1 s XPS spectra (Fig. S19) and the full wide XPS spectra (Fig. S20). The valence state change of Bi during the electrochemical process is additionally characterized by *ex-situ* Bi 4f XPS spectra (Fig. 4d). Compared with the initial state, most of Bi^{3+} and Bi are converted into Bi_2Mg_3 at the fully discharged state (0.01 V). At 1.2 V (the fully charged state), the intensity of peaks corresponding Bi metal increases, indicating that the dealloying process of Bi_2Mg_3 occurs during the charging. Partial irreversible reactions lead to the presence of the Bi_2Mg_3 peak at the charged state, which can provide an explanation for the low Coulombic efficiency at the first cycle and the observed Mg1s peak at the charged state. *Ex-situ* XPS spectra of Bi 4f for BOC additionally indicate the formation of Bi and Bi_2Mg_3 (Fig. S21).

The morphology and structural changes of Bi@NC during charge and discharge are further studied by *ex-situ* TEM. The TEM image of Bi@NC (Fig. 4e) at the discharged state indicates that Bi nanoparticles undergo fragmentation, which may be attributed to the significant volume changes resulting from alloying reactions. However, the fragmented Bi nanoparticles are still well-encapsulated by the carbon shell, effectively preventing the loss of active material. Distinct lattice fringes are clearly visible in the high-resolution TEM (HRTEM) images of Bi@NC (Figs. 4f and S22). Lattice spacings of 4.07 Å and 2.34 Å correspond to the (100) and (110) crystal planes of Bi_2Mg_3, respectively. While lattice spacings of 3.26 Å and 3.25 Å correspond to the (012) crystal planes of Bi. At the charged state, the morphology of Bi@NC, as depicted in Fig. 4g, exhibits no significant changes, and distinct lattice fringes are still observable in the HRTEM images (Fig. 4h and Fig. S23). Lattice spacings of 3.75 Å, 3.25 Å and 1.97 Å correspond to the (101), (012) and (006) crystal planes of Bi, respectively. Lattice spacing of 2.75 Å correspond to the (102) crystal planes of Bi_2Mg_3. The elemental maps of Bi@NC at fully discharged state (0.01 V) (Fig. 4i) and EDX spectrum (Fig. S24) also demonstrate the insertion of Mg^{2+} ions. The signal of Mg element for the charged Bi@NC is significantly weakened (Fig. S25 and S26), which confirms the deinsertion of Mg^{2+} ions. The results from *ex-situ* TEM further confirm

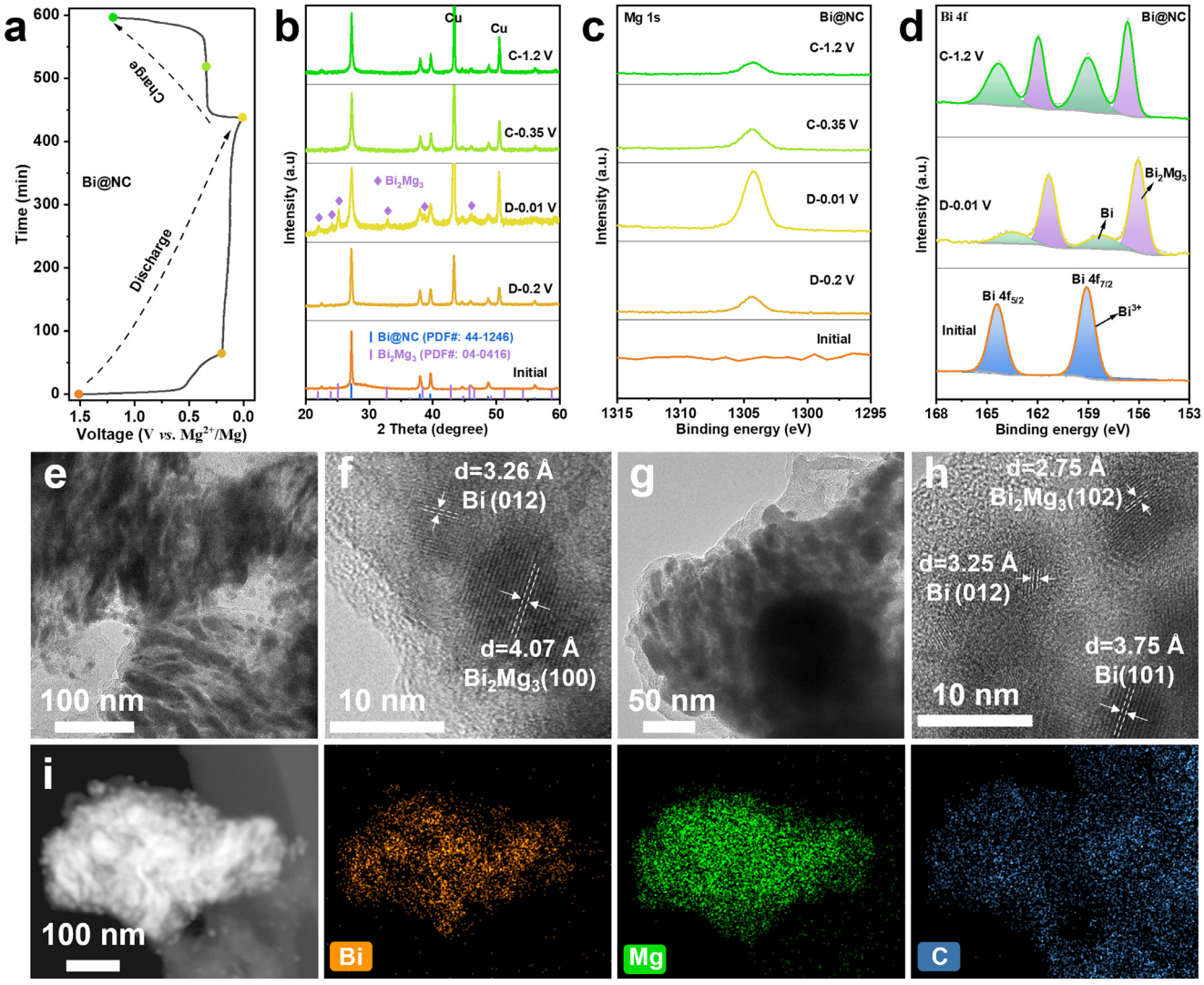

Fig. 4. (a) and (b) *Ex-situ* XRD patterns of Bi@NC at different charge or discharge states. (c) *Ex-situ* XPS spectra of (c) Mg 1 s and (d) Bi 4f for Bi@NC at different states. TEM image (e) and HRTEM image (f) of Bi@NC at fully discharged state (0.01 V). TEM image (g) and HRTEM image (h) of Bi@NC at fully charged state (1.2 V). (i) HAADF image and corresponding elemental maps of Bi@NC at fully discharged state (0.01 V).

the Mg^{2+} storage mechanism of Bi@NC based on alloying reactions, consistent with the results obtained from *ex-situ* XRD and XPS.

4. Conclusions

In summary, we have successfully prepared Bi nanoparticles encapsulated in nitrogen-doped carbon with single-atom Bi embedded by low temperature calcination method. The atomic arrangement of Bi metal and the distribution of single-atom Bi are revealed through spherical aberration-corrected STEM. The coating state and form of carbon in Bi@NC are deeply analyzed by 3D tomography reconstruction techniques. Furthermore, we have evaluated the magnesium storage performance of Bi@NC as an anode material for MBs in a fluoride alkyl Mg salt electrolyte. At 100 mA g^{-1}, Bi@NC exhibits a high discharge capacity of 347.5 mAh g^{-1}. Even at 500 mA g^{-1}, Bi@NC has a capacity of 263.4 mAh g^{-1} and 82.5% capacity retention after 400 cycles. Compared with reported Bi and Bi-based compound anodes for MBs, Bi@NC exhibits the longest cycle life. Finally, the magnesium storage mechanism of Bi@NC is shown to involve an alloying reaction from Bi to Bi_2Mg_3 by *ex-situ* XRD, XPS and TEM. This work demonstrates that electrolyte formulations have a huge impact on electrode material performance, and the compatibility of electrolytes and electrode materials should also be considered while designing the structure of electrode materials.

Declaration of competing interest

The authors declare that they have no known competing financial interests or personal relationships that could have appeared to influence the work reported in this paper.

CRediT authorship contribution statement

Junjun Wang: Conceptualization, Formal analysis, Investigation, Methodology, Writing – original draft, Writing – review & editing. **Ruohan Yu:** Formal analysis, Investigation, Methodology. **Jianxiang Wang:** Data curation, Formal analysis, Investigation. **Juncai Long:** Data curation, Investigation. **Fan Qiao:** Formal analysis, Investigation, Writing – review & editing. **Lei Zhang:** Investigation, Writing – review & editing. **Guanjie He:** Formal analysis, Investigation, Writing – review & editing. **Qinyou An:** Conceptualization, Formal analysis, Investigation, Project administration, Supervision, Writing – review & editing. **Liqiang Mai:** Conceptualization, Funding acquisition, Project administration, Supervision, Writing – review & editing.

Acknowledgments

Junjun Wang and Ruohan Yu contributed equally to this work. This work was supported by the National Natural Science Foundation of China (51972259, 52127816, and 52202290), the National Key Research and Development Program of China (2020YFA0715000), the Natural Science Foundation of Hubei Province (2022CFA087). Junjun Wang thanked the funding support from China Scholarship Council/University College London for the joint Ph.D. scholarship (CXXM2110070005).

Supplementary materials

Supplementary material associated with this article can be found, in the online version, at doi:10.1016/j.jma.2023.10.001.

References

[1] Y. Liang, H. Dong, D. Aurbach, Y. Yao, Nat. Energy 5 (2020) 646–656.
[2] Z. Li, J. Häcker, M. Fichtner, Z. Zhao-Karger, Adv. Energy Mater. 13 (2023) 2300682.
[3] S. Tan, F. Xiong, J. Wang, Q. An, L. Mai, Materials Horizons 7 (2020) 1971–1995.
[4] F. Liu, T. Wang, X. Liu, L.Z. Fan, Adv. Energy Mater. 11 (2021) 2000787.
[5] X. Ren, F. Wen, S. Cao, F. Xu, Chem. Eng. J. 452 (2023) 139570.
[6] J. Wang, S. Tan, G. Zhang, Y. Jiang, Y. Yin, F. Xiong, Q. Li, D. Huang, Q. Zhang, L. Gu, Q. An, L. Mai, Sci. China Mater. 63 (2020) 1651–1662.
[7] R. Attias, M. Salama, B. Hirsch, Y. Goffer, D. Aurbach, Joule 3 (2019) 27–52.
[8] S. Hou, X. Ji, K. Gaskell, P.f. Wang, L. Wang, J. Xu, R. Sun, O. Borodin, C. Wang, Science 374 (2021) 172–178.
[9] J. Wen, J. Yang, X. Huang, X. Zhang, G. Huang, J. Wang, L. Li, F. Pan, J. Magnes. Alloys (2023), doi:10.1016/j.jma.2023.06.007.
[10] D. Zhang, S. Duan, X. Liu, Y. Yang, Y. Zhang, W. Ren, S. Zhang, M. Cheng, W. Yang, J. Wang, Y. NuLi, Nano Energy 109 (2023) 108257.
[11] F. Wang, H. Hua, D. Wu, J. Li, Y. Xu, X. Nie, Y. Zhuang, J. Zeng, J. Zhao, ACS Energy Lett 8 (2023) 780–789.
[12] S.B. Son, T. Gao, S.P. Harvey, K.X. Steirer, A. Stokes, A. Norman, C. Wang, A. Cresce, K. Xu, C. Ban, Nat. Chem. 10 (2018) 532–539.
[13] B. Wan, H. Dou, X. Zhao, J. Wang, W. Zhao, M. Guo, Y. Zhang, J. Li, Z.F. Ma, X. Yang, ACS Appl. Mater. Interfaces 12 (2020) 28298–28305.
[14] J. Niu, Z. Zhang, D. Aurbach, Adv. Energy Mater. 10 (2020) 2000697.
[15] F. Zhang, Y. Shen, H. Xu, X. Zhao, ACS Appl. Mater. Interfaces 15 (2023) 23353–23360.
[16] M. Song, T. Zhang, J. Niu, H. Gao, Y. Shi, Y. Zhang, W. Ma, Z. Zhang, J. Power Sources 451 (2020) 227735.
[17] L. Wang, S.S. Welborn, H. Kumar, M. Li, Z. Wang, V.B. Shenoy, E. Detsi, Adv. Energy Mater. 9 (2019) 1902086.
[18] T.S. Arthur, N. Singh, M. Matsui, Electrochem. Commun. 16 (2012) 103–106.
[19] Z. Liu, J. Lee, G. Xiang, H.F. Glass, E.N. Keyzer, S.E. Dutton, C.P. Grey, Chem. Commun. 53 (2017) 743–746.
[20] T.R. Penki, G. Valurouthu, S. Shivakumara, V.A. Sethuraman, N. Munichandraiah, New J. Chem. 42 (2018) 5996–6004.
[21] J. Niu, H. Gao, W. Ma, F. Luo, K. Yin, Z. Peng, Z. Zhang, Energy Storage Mater. 14 (2018) 351–360.
[22] J. Niu, K. Yin, H. Gao, M. Song, W. Ma, Z. Peng, Z. Zhang, Nanoscale 11 (2019) 15279–15288.
[23] S. Chen, Y. Du, H. Ma, Z. Wang, S. Fan, W. Zhang, H.Y. Yang, Nano Lett (2023).
[24] C. Zhu, Y. Tang, L. Liu, X. Bai, Y. Xu, Y. Nuli, J. Wang, Mater. Horiz. 10 (2023) 1719–1725.
[25] W. Wang, L. Liu, P.F. Wang, T.T. Zuo, Y.X. Yin, N. Wu, J.M. Zhou, Y. Wei, Y.G. Guo, Chem. Commun. 54 (2018) 1714–1717.
[26] Y.H. Tan, W.T. Yao, T. Zhang, T. Ma, L.L. Lu, F. Zhou, H.B. Yao, S.H. Yu, ACS Nano 12 (2018) 5856–5865.
[27] Y. Shao, M. Gu, X. Li, Z. Nie, P. Zuo, G. Li, T. Liu, J. Xiao, Y. Cheng, C. Wang, J.G. Zhang, J. Liu, Nano Lett. 14 (2014) 255–260.
[28] B.Z. Lu Wang, Bin Wang, Suyuan Zeng, Mingwen Zhao, Xiuping Sun, Yanjun Zhai, Liqiang Xu, Angew. Chem. Int. Ed. 133 (2021) 15509–15517.
[29] J. Xiang, Z. Liu, T. Song, ChemistrySelect 3 (2018) 8973–8979.
[30] J. Long, S. Tan, J. Wang, F. Xiong, L. Cui, Q. An, L. Mai, Angew. Chem., Int. Ed. 62 (2023) e202301934.
[31] S. Wei, W. Li, Z. Ma, X. Deng, Y. Li, X. Wang, Small (2023) e2304265.
[32] Z. Hao, X. Shi, W. Zhu, X. Zhang, Z. Yang, L. Li, Z. Hu, Q. Zhao, S. Chou, Chem. Sci. 13 (2022) 11376–11381.
[33] V. Augustyn, J. Come, M.A. Lowe, J.W. Kim, P.L. Taberna, S.H. Tolbert, H.D. Abruña, P. Simon, B. Dunn, Nat. Mater. 12 (2013) 518–522.